Study of densification mechanisms during Spark Plasma Sintering of co-precipitated Ho:Lu2O3 nanopowders: Application to transparent ceramics for lasers

Lucas Viers, Florian Delaunay, Rémy Boulesteix, Marion Vandenhende, Guy Antou, Alexandre Maître

Version of Record: https://www.sciencedirect.com/science/article/pii/S0955221921004982
Manuscript_518c1b5d321197671eed0d167ee8d0df

Study of densification mechanisms during Spark Plasma Sintering of co-precipitated Ho:Lu_2O_3 nanopowders: application to transparent ceramics for lasers.

Lucas Viers[1], Florian Delaunay[1], Rémy Boulesteix[1*], Marion Vandenhende[1], Guy Antou[1], Alexandre Maître[1]

[1] Institute for Research on Ceramics (IRCER), UMR CNRS 7315, Univ. Limoges, F-87068 Limoges, FRANCE

Abstract

This work was focused on the determination of densification mechanisms during Spark Plasma Sintering (SPS) of Ho:Lu_2O_3 nanopowders. Strong variation of the stress exponent n was evidenced during the sintering process. At low relative density (*i.e.* $\rho < 66\%$), n=3 and powder particles rearrangement and **coalescence** take place because of high value of effective stress **and low size of primary nanoparticles**. Then, for ρ between 66% and 85%, the stress exponent decreases to $n = 2$ then n = 1. Such values were related to Rachinger then Lifshitz sliding mechanisms, the last one was associated with an average activation energy of 565 $kJ.mol^{-1}$. At the final densification stage ($\rho > 85\%$), the stress exponent suddenly increases to 4 in accordance with a power-law creep. From these investigations, an optimized thermomechanical cycle was proposed to obtain highly transparent Ho:Lu_2O_3 ceramics suitable for laser applications.

Keywords : Densification mechanisms ; Stress exponent ; Effective stress ; Spark Plasma Sintering ; Transparent ceramics ; Nanopowder

1. Introduction

For a decade, 2 µm active laser ceramics have been mainly studied for their great potential in high power applications **[1][2]** and more particularly for medical field because of absorption band of water at this wavelength **[3][4]**. Among 2 µm emitting ions, Ho^{3+} presents the largest emission cross-section which allows its use as efficient active ion for solid-state lasers **[5]**. Garnet structures like Yttrium Aluminum Garnet (YAG) are widely used as host matrix **[6-8]** for laser ions. However, some studies have shown that rare-earth sesquioxides (Sc_2O_3, Y_2O_3 and Lu_2O_3) present some advantages in comparison to YAG **[9][10]**. More precisely, they exhibit a higher thermal conductivity, and Lu_2O_3 keeps enhanced thermal conductivity for high concentration of Ho^{3+} ions **[11]**. Unfortunately, this compound has a very refractory behavior ($T_{melting}$ = 2450°C against 1980°C for YAG), so pressure-assisted sintering methods are needed to reach a fully dense and transparent material such as Hot Isostatic Pressing (HIP) **[12]** or Spark Plasma Sintering (SPS) **[13]**.

Spark Plasma Sintering is often used for the manufacturing of nanocrystalline refractory ceramics **[14]** because of its numerous advantages including short heat treatments, very fast densification and limited grain growth **[15]**. But the physical-chemistry mechanisms occurring in the green compact during the heat treatment and leading to a fast shrinkage are still under debate **[16][17]**, as same as the effect on grain growth **[18]**. In order to identify the related densification mechanisms, some analytical models have been developed and applied to the experimental data obtained from SPS measurements **[19]**. One of them is the G.-Bernard-Granger's approach (GBG model), often used for ceramic oxides **[20][21].** It is based on the determination of the stress exponent at a given thermomechanical treatment. This model allows to draw conclusions on densification controlling mechanism by estimating the effective stress applied on the powder compact thanks to an analytical expression developed by Coble for HIP configuration **[22]**. Nevertheless, this GBG approach suffers from the strong

dependence of the thus-identified values of densification parameters (*i.e.* stress exponent and apparent activation energy) on the precise evaluations of the effective stress acting on the powder bed. Another approach, suggested in a previous paper by G. Antou *et al.* **[23]**, consists in comparing the normalized shrinkage rates in isothermal and isobar conditions at fixed microstructural features, especially at given relative density. Therefore, by applying different macroscopic stresses, the comparison of shrinkage rates at fixed density allows identifying the stress exponent value, and finally its potential evolution during the densification process. This model was applied to the study of SPS densification behavior on alumina and was compared with densification by Hot Pressing (HP) **[23]**. The obtained results for both sintering ways were compared with corresponding creep tests at high temperature. Proposed densification mechanisms were in good agreement with microstructural observations and it was demonstrated the robustness of this new approach.

The aim of this work is to confirm consistency of this second model to SPS sintering of Ho:Lu_2O_3 ceramics. The corresponding shrinkages have been obtained under different thermomechanical cycles. Experimental conditions were designed to make varying in a large extent the effective stress and temperature applied to the powder compact. As a result, stress exponent and apparent activation energy values for densification will be identified. These densification parameters will be correlated with microstructural observations before drawing conclusions on involved densification mechanism and its evolution. Finally, the conclusions of the model will be used to define optimized sintering schedule in order to obtain fully dense and transparent Ho:Lu_2O_3 ceramics.

2. Experimental

2.1. Synthesis of Ho:Lu_2O_3 nanopowders

Ho-doped Lu_2O_3 nanopowders were synthesized by inverse co-precipitation route using rare-earth nitrates as precursor and ammonium bicarbonate as precipitant. Commercial oxides

of Lu_2O_3 and Ho_2O_3 (AUER REMY, Lehvoss group, Hamburg, Germany) were first dissolved in nitric acid (HNO_3, 65 vol.%, Thermo Fisher Scientific, Waltham, Massachusetts, USA). The nitrate solution was poured into a solution of ammonium bicarbonate (NH_4HCO_3, 99wt.%, Acros Organics, Thermo Fisher Scientific, Waltham, Massachusetts, USA) at a rate of 3 $mL.min^{-1}$ with vortex stirring. The pH was maintained at 9 by adding ammonia solution (NH_4OH, 35vol.%, Thermo Fisher Scientific, Waltham, Massachusetts, USA). Then the solution was aged for 24 h under stirring at room temperature. The obtained precipitate was washed by centrifugation three times with water and three times with ethanol and was dried at 70°C. The dried precipitate was milled in an agate mortar and calcined at 1000°C for 2 h under air to form the final 1at.%Ho:Lu_2O_3 nanopowder. Powder morphology, chemical homogeneity and structure were obtained by TEM (Transmission Electronic Microscopy), High-resolution TEM coupled with SAED (Selected Area Electron Diffraction) and STEM (Scanning Transmission Electronic Microscopy) (2100F, JEOL, Tokyo, Japan). Figure 1 shows a slightly edged shape and narrow size distribution of particles with mean diameter of about **63 nm**. Particles also appear well crystallized in the well-known bixbyite structure (Ia-3, cubic C-type) as revealed by diffraction pattern (Figure 1b). Also, no holmium segregation was detected as illustrated by STEM micrographs in Figure 1c,d. As a result, the Ho:Lu_2O_3 powder can be considered as a $Lu_{(2-x)}Ho_xO_3$ homogeneous solid-solution (x = 0.02 for 1at.% holmium doping content) with cubic crystalline structure.

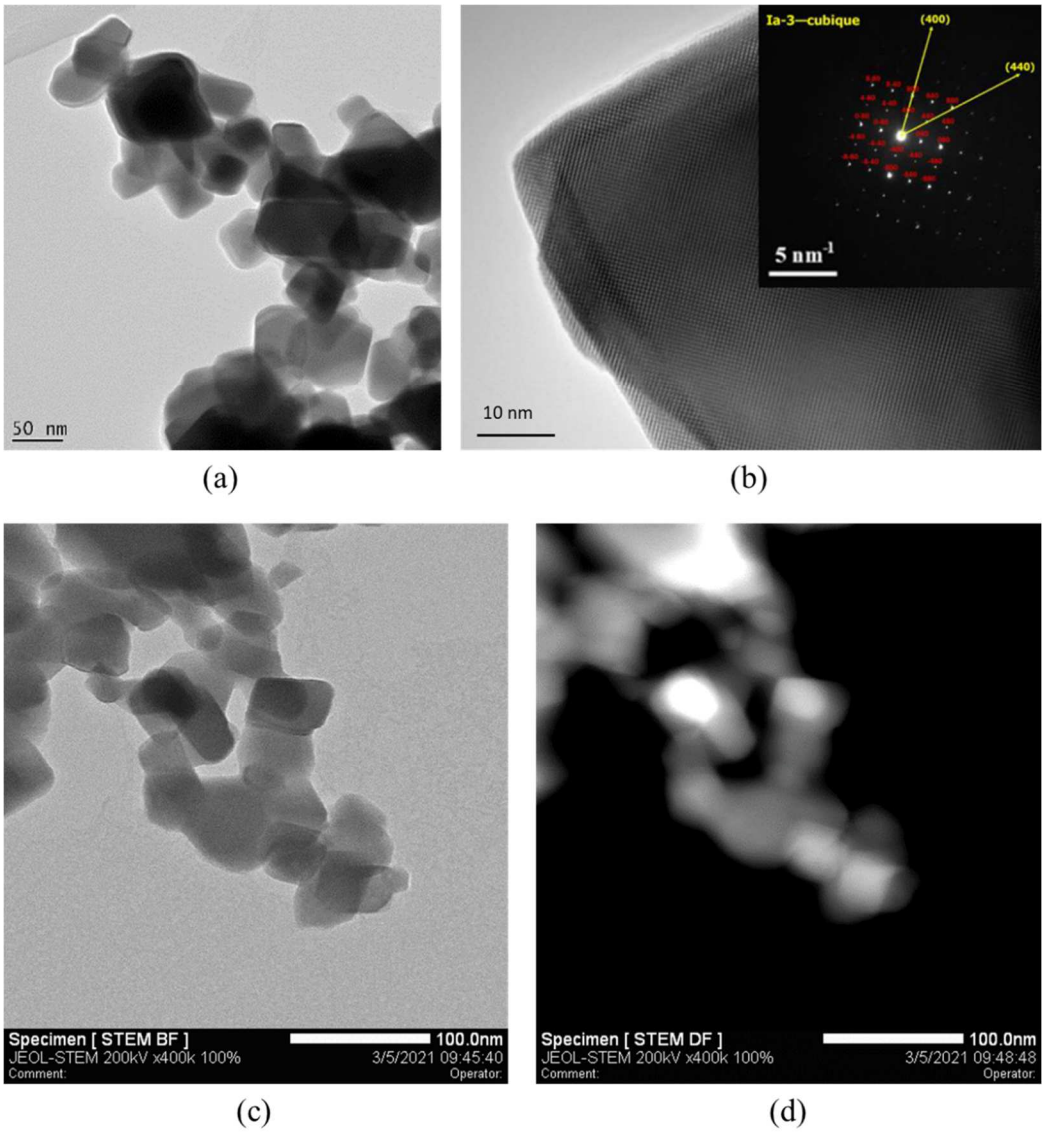

Figure 1. TEM (a), high-resolution TEM with corresponding diffraction pattern (b), STEM in bright field (c) and STEM in dark field (d) micrographs of the co-precipitated 1at.%Ho:Lu_2O_3 powder calcined at 1000°C.

2.2. Densification by Spark Plasma Sintering

SPS experiments were achieved using a commercial device (825 serie 8000 A, FUJI-SPS, Saitama, Japan) under primary vacuum (P < 20 Pa) with a pulse sequence 12:2. The synthesized powder was put in a 13 mm diameter graphite die with Papyex® foil (MERSEN, La Défense, France). Thermal regulation was operated by a digital IR pyrometer on the surface of the graphite die with lower temperature detection limit at 573°C.

For all treatments used for the determination of mechanisms, the heating rate was fixed to 100°C.min^{-1} after a regulation dwell at 600°C for 2 min and was decreased 30°C before the soaking dwell to 50°C.min^{-1} to avoid a high thermal overshoot. The stress was applied in 2 min from the end of the regulation dwell whatever the thermomechanical cycle. The range of dwell time was **10-20 min**. For each sintering schedule, a blank was performed on the obtained fully dense sample to suppress thermoelastic response of the graphite system to the recorded displacement data. The Figure 2 summarizes the thermomechanical cycle **for a 20 min dwell time**.

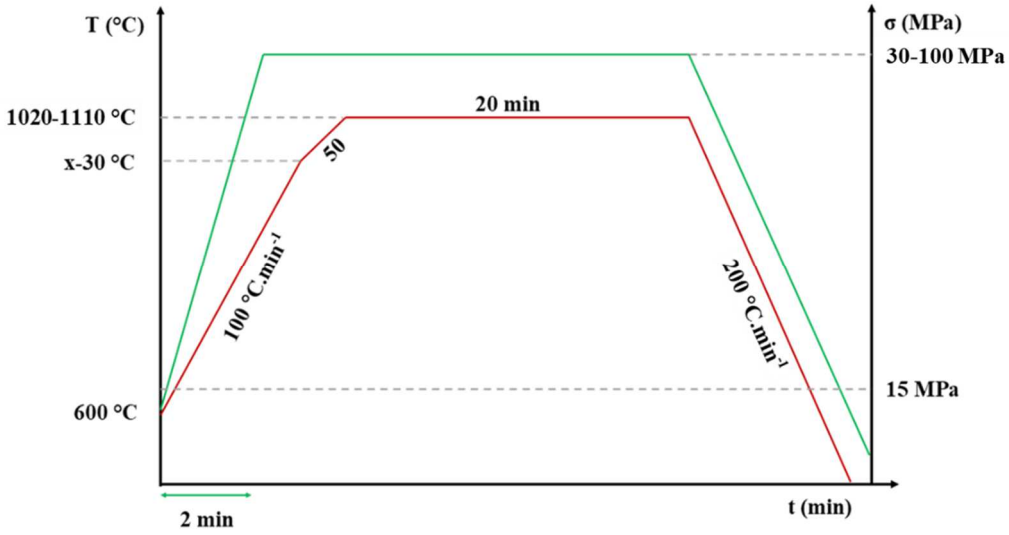

Figure 2. Scheme of the thermomechanical cycle used for SPS experiments.

2.3. Characterization of sintered samples

To determine the instantaneous relative density during the entire isothermal dwell, the following equation was applied on SPS displacement measurements:

$$\rho(t) = \rho_f \cdot \frac{h_f}{h(t)} \quad (1)$$

where $\rho(t)$ is the instantaneous relative density, ρ_f is the final relative density measured by Archimedes method in absolute ethanol (with temperature correction of liquid density), h_f the thickness of sintered sample, $h(t)$ the instantaneous thickness of the sample during sintering from lower piston displacement. The computation of the average grain size of sintered ceramic samples was performed on a minimum of 300 grains (obtained from at least three different FESEM micrographs) by grains contouring and treatment on ImageJ software (ImageJ, NIMH, Bethesda, Maryland, USA). The equivalent disc area diameter and an intensification factor of 1.56 was used to obtain the equivalent grain diameter G and mean grain diameter G_{mean} **[24]**. The transmission curves were obtained from transparent samples on a Cary 5000 (Agilent, Santa Clara, California, USA). Samples were mirror-polished by colloidal silica of 30 nm after pre-polishing with SiC papers and diamond slurries. The spectra resolution was 1 nm with an integration time equals to 0.1 s.

3. Results and discussion

3.1. Sintering trajectories

At first, samples microstructure was observed by SEM as a function of the thermomechanical cycle parameters. An example of such observations is given in Figure 3**.** From these micrographs, it is clear that not only densification, but also significant grain growth occur during SPS treatment. The grains appeared to be separated by well-defined grain boundaries, allowing determining the grain size with pretty good accuracy. The porosity is located at triple points and/or at grain boundaries, indicating that its elimination should be linked to classical densification mechanisms.

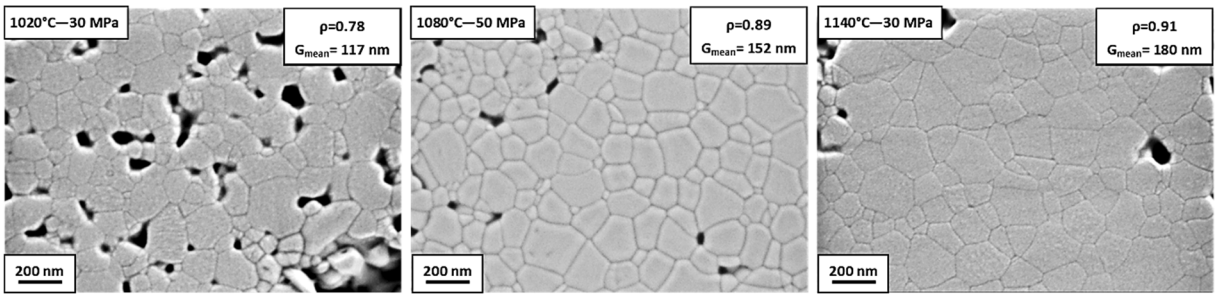

Figure 3. SEM micrographs illustrating the microstructural evolution of SPS samples from 1020°C to 1140°C and from 30 MPa to 50 MPa.

Average grain size (G_{mean}) and relative density (ρ) of Lu_2O_3 ceramics were obtained for different thermomechanical conditions during SPS treatment (Table 1). **It should be noted here that the initial mean grain size G_0 (*i.e.* powder particles diameter) is 63 nm and initial relative density ρ_0 (*i.e.* compacted powder compacity before sintering) is around 55% of the theoretical density**.

P = 30 MPa	T° - t *(°C – min)*	1020-20	1080-20	1140-20	1300-15	1500-20	-
	ρ (%)	78	84.5	90.6	97.2	100	-
	G_{mean} (nm)	117	137	180	299	651	-
P = 50 MPa	T° - t *(°C – min)*	963-20	1020-20	1080-20	1140-20	1427-10	1450-20
	ρ (%)	72.4	82.2	89.3	96.5	99.3	100
	G_{mean} (nm)	114	129	152	175	508	526
P = 100 MPa	T° - t *(°C – min)*	1000-20	1080-20	1140-10	1310-10	-	-
	ρ (%)	85.8	98.3	98.7	99.5	-	-
	G_{mean} (nm)	100	130	210	246	-	-

Table 1: Microstructural features of Lu_2O_3 ceramics as a function of thermomechanical parameters used during SPS sintering.

Figure 4a and b illustrate the *G = f(T,P)* and *ρ = f(T,P)* dependence from data reported in Table 1. It first appears a non-dependence of grain growth as a function of load in the investigated T-P domain. On the pressure effect during SPS, both non-dependence or positive dependence have already been reported for alumina, zirconia

and TaC [25]. For the positive dependence of grain growth, one can consider that the pressure effect can start to be significant at temperatures where the grain-boundary mobility is sufficiently high [26]. In the case of Ho:Lu_2O_3, grain growth starts to be rapid for temperatures higher than 1300°C as exposed in Figure 4b. This temperature almost represents the upper limit of the temperature range reported in Figure 4a, the obtained results are thus consistent with the literature.

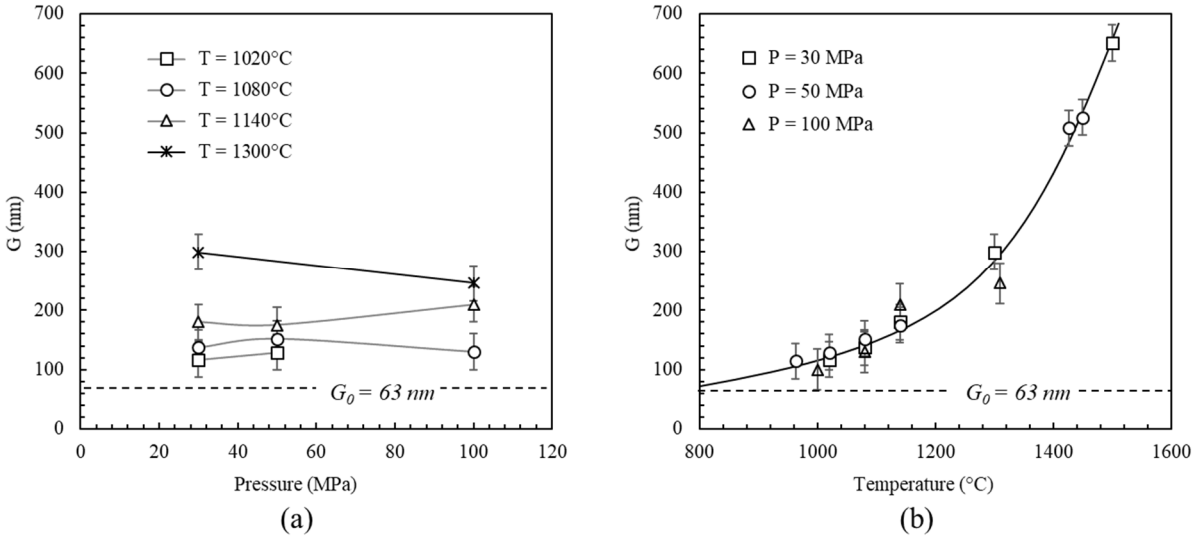

Figure 4 : Evolution of grain size as a function of uniaxial load at fixed temperature (a), or as a function of temperature at fixed load (b).

Second, it is clearly illustrated in Figure 5 the positive effect of increasing load on densification kinetics. According to the fact that G does not depend on P values in the studied P-T domain, the densification rate can be expressed as a function of load only.

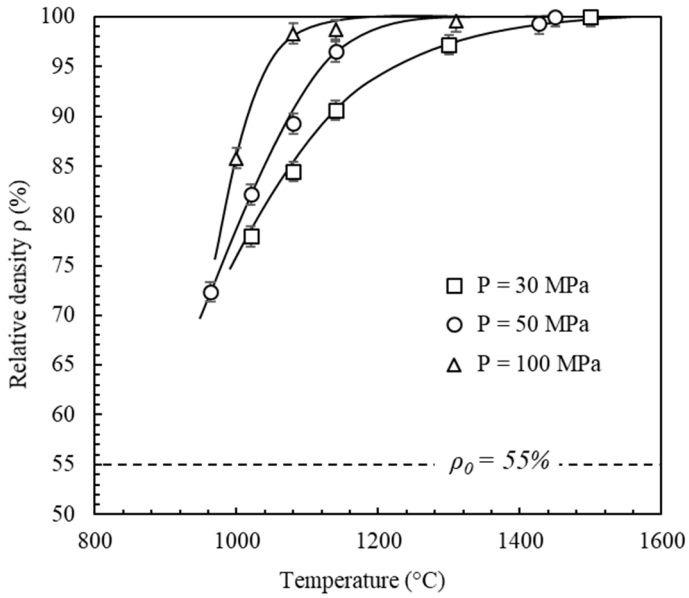

Figure 5 : Evolution of relative density as a function of temperature at fixed load.

Before comparing and analyzing the shrinkage rates evolution, sintering trajectories $G_{mean} = f(\rho)$ were plotted in Figure 6 to determine the domains of densification and coarsening stages. To obtain the stress exponent values, the model will be applied only where densification is predominant over grain growth. Therefore, in these conditions, the increase of G can been neglected in the model. At 100 MPa, grain growth occurs tardily at 97% of relative density, whereas it occurs at 92% for 50 MPa and around 88-90% for 30 MPa. So, the increase of applied stress permits to delay grain growth and to limit the average grains diameter. It is clear that high pressures lead to an increase of the ratio between densification rate and grain growth rate.

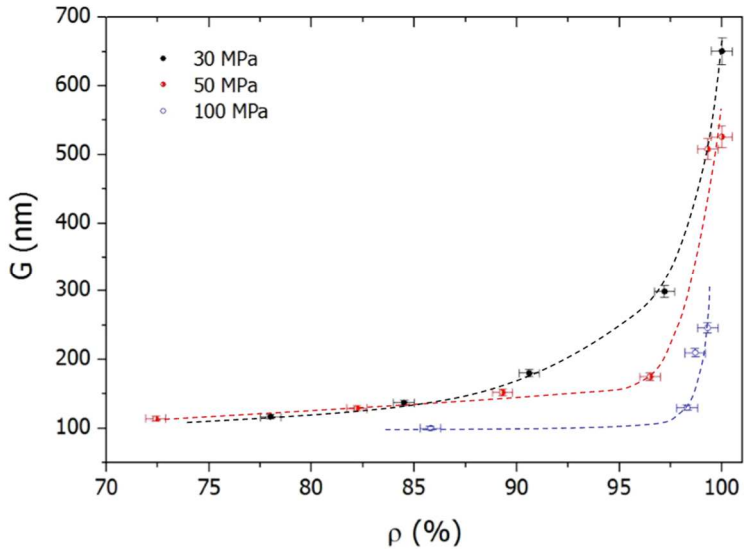

Figure 6. Sintering trajectories G-ρ of Ho:Lu_2O_3 ceramics during SPS at constant pressures of 30 MPa, 50 MPa and 100 MPa.

Thanks to these observations, the determination of densification mechanisms will be more accurate for relative density below 90%, *i.e.* where grain growth contribution could be neglected. Moreover, Ho^{3+} is isovalent of Lu^{3+} and no holmium segregation was detected in the samples. Thus Ho:Lu_2O_3 ceramics were considered as a $Lu_{(2-x)}Ho_xO_3$ (x = 0.02 for 1at.% holmium doping content) homogeneous solid-solution with cubic crystalline structure. As a result, holmium was considered to have no specific influence on Ho:Lu_2O_3 sintering mechanisms.

3.2. Stress exponent determination

To determine the value of stress exponent as a function of the applied stress in isothermal conditions, the equation (2) was used in absence of significant grain growth (*i.e.* $G_{mean} < 2G_0$, see section 3.1).

$$\frac{1}{\rho}\frac{d\rho}{dt} = B' \sigma_{zz}{}^{n} \qquad (2)$$

where $\frac{d\rho}{dt}$ is the densification rate, B' a constant depending on relative density and σ_{zz} the macroscopic applied stress.

The equation (2) becomes equation (3) by applying a natural logarithm to extract the stress exponent **n:**

$$\ln\left(\frac{1}{\rho}\frac{d\rho}{dt}\right) = \mathbf{n}\ \ln\sigma_{zz} + \ln(B') \quad (3)$$

Thus, by plotting the evolution of $\ln\left(\frac{1}{\rho}\frac{d\rho}{dt}\right)$ for the same relative density ρ as a function of $\ln(\sigma_{zz})$ with a minimum of 3 values, it is possible to determine the value of the stress exponent from the slope coefficient of the straight line obtained. Constant relative density will permit to extract n at fixed microstructure. In addition, obtaining a straight line can constitute an additional element of validation of this model.

Heat treatments were carried out at four temperatures (from 1020°C to 1110°C) and three different macroscopic stresses (30 MPa, 40 MPa and 50 MPa). Densification curves in Figure 7A were obtained by fitting treatment of experimental data from SPS displacement measurements.

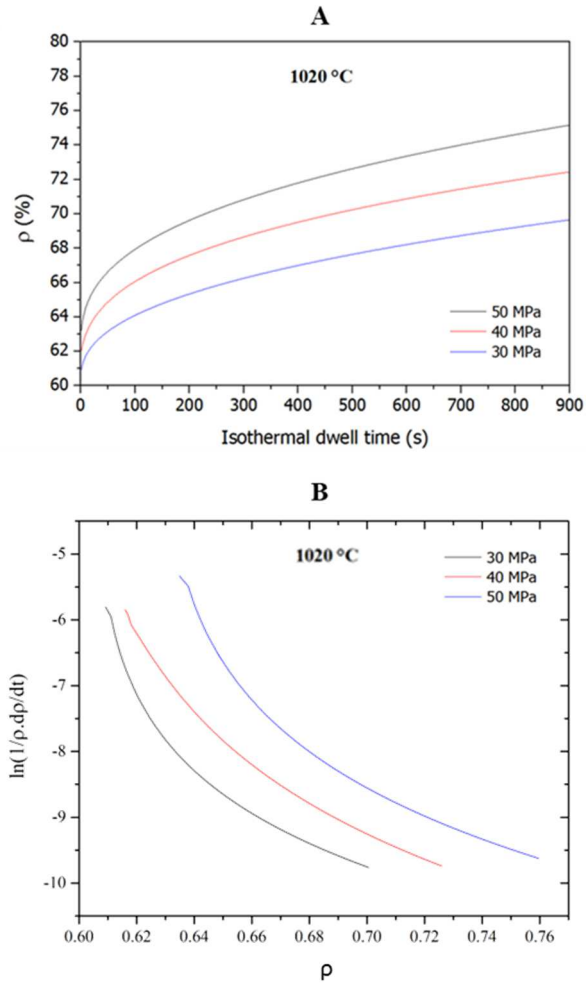

Figure 7. A. Densification curves at 1020°C and under different applied stresses (30 to 50 MPa), B. derivation and normalization of densification curves as a function of relative density.

As a result, it is possible to obtain the value of stress exponent from the slope of the line, and finally to get the possible mechanism acting on densification. All these results (example for one temperature in Figure 8) confirms the reliability of this model by the linear fit of all data at different temperatures. Moreover, the hypothesis of an invariant microstructure (*i.e.* limited grain growth) has been previously checked. The maximal standard deviation obtained is under 10%.

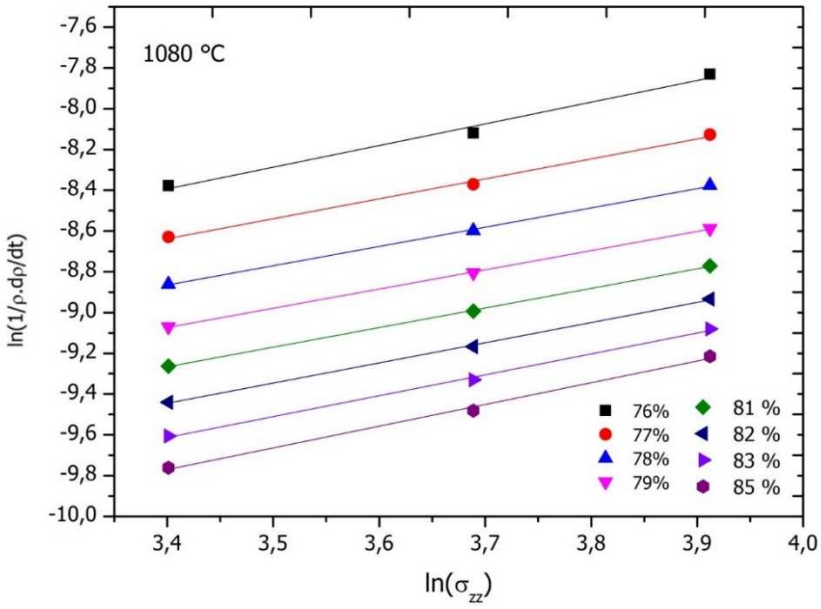

Figure 8. Determination of stress exponent associated to a relative density by plotting in a logarithmic scale the shrinkage rate as a function of stress.

The Figure 9 summarizes all stress exponent values obtained from linear fits. At low relative density (*i.e.* ρ < 67%), the stress exponent is above 3. Its value progressively decreases to reach a plateau at a value close to 1 from ρ = 76% to 85%. For higher values of relative density, the stress exponent rapidly increases to values close to 3 or even higher.

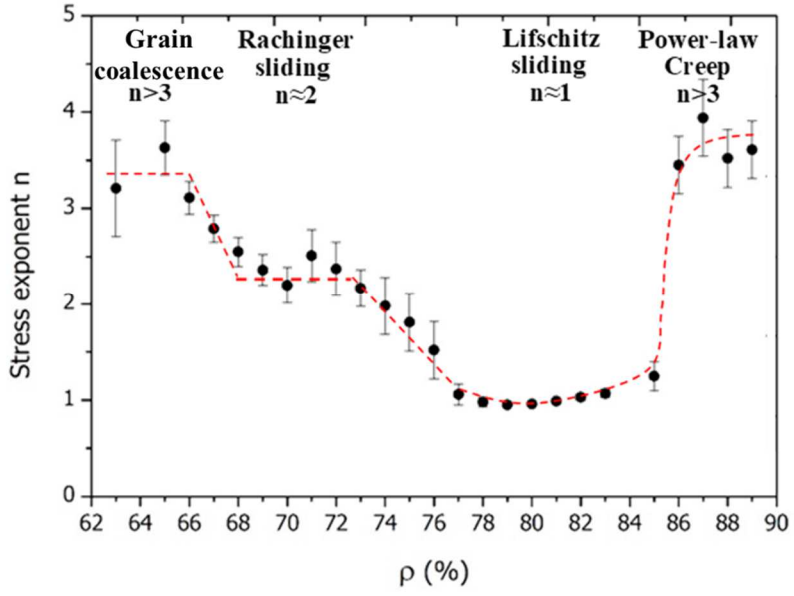

Figure 9. Evolution of stress exponent with relative density of Ho:Lu_2O_3 ceramics during SPS from 1020°C to 1110°C.

From Figure 9, a high value of stress exponent was registered for low relative density. That means the densification rate is very sensitive to the applied stress. Such behaviour can be explained by **grains coalescence and rearrangement** caused by the high stress perceived by nanograins, namely the effective stress σ_{eff}, given by Eq. (4) from Helle stacking model **[22]**.

$$\sigma_{eff} = \frac{1 - \rho_0}{\rho^2 (\rho - \rho_0)} \sigma_{zz} \quad (4)$$

where ρ_0 is the initial relative density (*i.e.* green compacity) and σ_{zz} the applied macroscopic stress in z direction. The Figure 10 plots an estimation of the evolution of σ_{eff} with the relative density for different applied stresses σ_{zz} according to Eq. (4). For low relative density domain where the stress exponent is around 3, the effective stress appears to be at least 4 times higher than the applied macroscopic stress and reaches for example 300 MPa for ρ = 63% and σ_{zz} = 50 MPa. Such value is **significantly lower** than the compressive strength reported for RE_2O_3 (RE = Y, Lu, Sc) based ceramics of 600-1000 MPa depending on temperature **[27]**. **At those high effective stresses and pretty low temperatures, small nanometric particles are prone to plastic deformation and/or coalescence [28,29]**. This phenomenon has been already observed by Chaim during SPS sintering of YAG [**30,31]** or MgO **[32]** nanopowders.

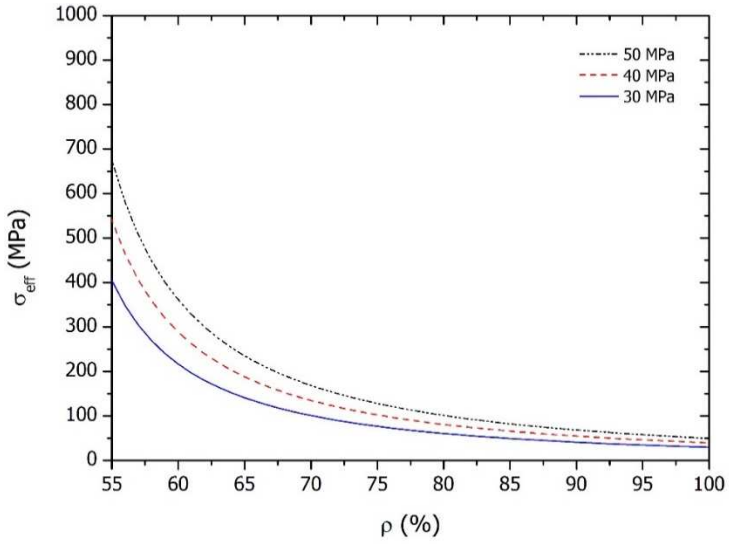

Figure 10. Evolution of effective stress with relative density from equation (4).

The observation of samples microstructure at early stage of densification as exposed in Figure 11(a) **shows grains with pretty large size distribution with diameters of around 20-40 nm to 120 nm at ρ = 0.7. As previously exposed in Figure 4b, it also appears that the measured grain size continuously increases with the temperature whatever the applied sintering schedule. Thus, the first stage of densification should be accompanied by grains rearrangement and coarsening/coalescence leading to rapid (but limited) grain growth. The mean grain diameter is in fact multiplied by a factor 2 between room temperature (initial grain size G_0 = 63 nm) and T = 1050°C (G_{mean} ≈ 120-130 nm). This agrees well with grains rearrangement and coalescence as the most probable and predominant mechanism during early stage of densification. Such rearrangement and coalescence could explain the concomitance of compacted areas constituted of small grains (black arrows in Figure 11(b)) surrounded by larger grains of 100-200 nm in diameter.**

At higher stage of densification, some residual extra (or "ghost") grain-boundaries inside the volume of bigger grains were identified by red arrows in Figure 11(b) and (c). **Such observation could result from grain coalescence at early stage of densification. In fact,**

one can observe that such phenomenon is only observed at the early and intermediate stage of densification (*i.e.* ρ < 0.9). At those sintering stages, temperature is limited to 900°C-1050°C but is high enough to initiate grain growth, whatever the applied load, as exposed in Figure 4b. Nevertheless, such temperature is probably too low to make all structural residual defects in grains volume (probably dislocations) being eliminated by solid-state diffusion. From SEM and TEM analyses performed on sintered samples (Figure 11(d) and Figure 11(e), respectively), ghost grain boundaries are no longer observed for temperatures above 1300°C, *i.e.* a temperature where grain growth and solid-state diffusion at grain scale must become significant.

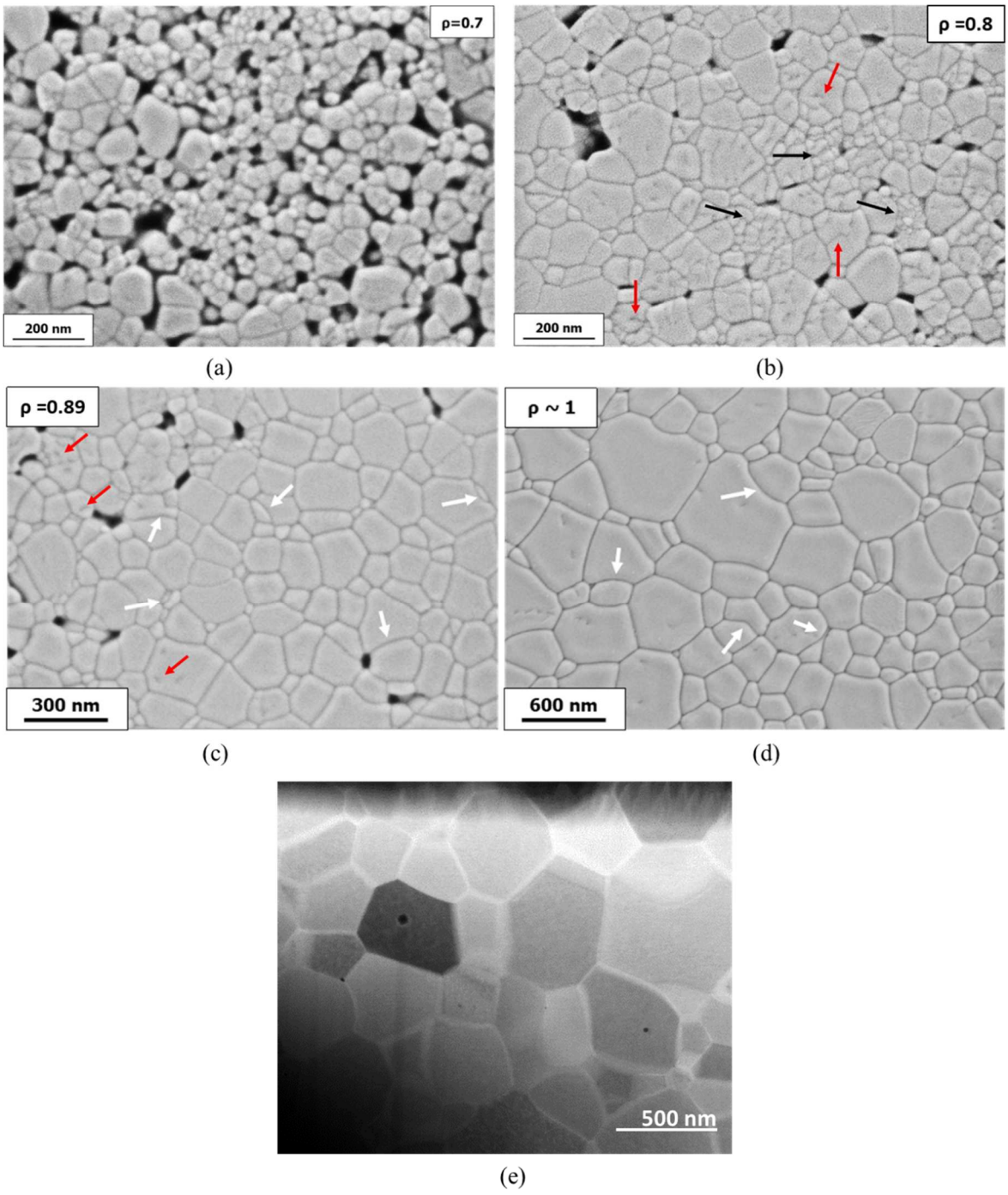

Figure 11. SEM micrographs of Lu_2O_3 ceramic samples after SPS under different thermomechanical treatments leading to ρ from 0.7 to 1. (a) early stage of densification showing nanometric particles ***under rearrangement and coalescence (black arrows)****, (b) and (c) intermediate stage of sintering showing* ***bigger grains with residual ghost grain boundaries (red arrows)****, (d) final stage of sintering (ρ ≈ 1) showing curved grain boundaries (white arrows) associated to significant grain growth* ***and (e) corresponding TEM micrograph.***

Also, due to densification, the effective stress decreases which can explain the decrease of the stress exponent to 2 for intermediate values of ρ (*i.e.* 67%-76% according to the Figure 9). In this sintering stage, the densification takes place without concomitant elongation of grains by Rachinger sliding in case of absence of a glassy phase **[33]**. In this case, elastic grains sliding phenomenon is accommodated by the presence of porosity at grain boundaries, as shown in Figure 11(a). When the stress exponent is equal to 1 for ρ from 76% to 85%, the local effective stress is accommodated by the denser microstructure. The effect of stress is less important than for low relative density because of the decrease of developed surface area due to the formation of necks and grain boundaries that is well illustrated by in Figure 11(b) and (c). During this stage, the supposed densifying mechanism should be controlled by diffusion kinetics of ionic species, involving a Lifshitz sliding, which explains the lower influence of applied stress on microstructure. In this process, similar to Nabarro-Herring or Coble creep, the grains morphology can evolve because of grain boundary sliding activated by intergranular flow diffusion. This point is supported by the observation of curved grain boundaries as pointed by white arrows in Figure 11(c) and (d).

Finally, the exponent rises abruptly to 3-3.5 for ρ > 85%. This final evolution indicates a change in densification controlling mechanism between the diffusion creep (n=1) and the power-law creep around 85% (n>3) **[34]**. According to previous studies **[24,33,35]**, a value of stress exponent greater than 3 even 4 means that densification is controlled by plastic deformation, generally limited by dislocation motion. Deeper characterization of samples, for example by high-resolution TEM, is needed to support this point.

3.3. Activation energy determination

For the first stage of sintering at low relative density, the densification phenomenon is mainly related to particle rearrangement accompanied with **coalescence**. To have an

analytical model of densification at this early stage of sintering, it could be interesting to introduce a physical component describing the particle rearrangement in a granular green body that should be much more sensitive to pressure than temperature. In such conditions, the determination of corresponding activation energy seems thus unsuitable. Nevertheless, it can be argued that the **rearrangement and coalescence** of grains observed at the early stage of sintering can contribute to explain the very fast densification generally observed during SPS experiments.

For $\rho > 75\%$, it seems possible to determine the corresponding activation energy at a given stress exponent value (*i.e.* 1 for the intermediate stage of densification). According to Equation (5), the apparent activation energy of densification can be obtained at fixed $\boldsymbol{\sigma_{zz}}$ and $\boldsymbol{\rho}$, *e.g.* at fixed pressure and similar microstructure, from the slope of the line obtained when $\ln\left(\frac{1}{\rho}\frac{d\rho}{dt}\right)$ is plotted as function of 1/T:

$$\ln\left(\frac{1}{\rho}\frac{d\rho}{dt}\right) = -\frac{\mathbf{E_a}}{RT} + C \qquad (5)$$

where E_a is the apparent activation energy of densification associated to the limiting mechanism, and C is a constant. These plots were reported in Figure 12. When n is close to 1 (*i.e.* $75\% < \rho < 85\%$ according to Figure 9), an average activation energy of 565±150 kJ.mol^{-1} is obtained.

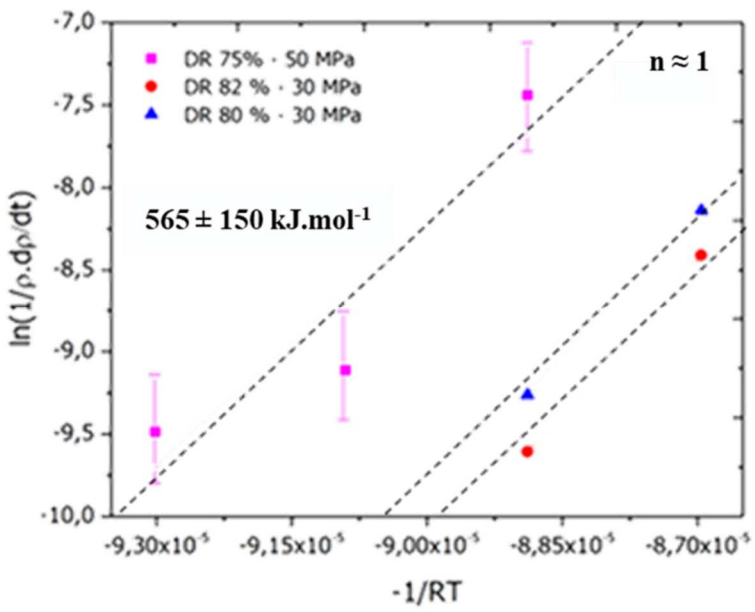

Figure 12. Determination of apparent activation energy of densification for diffusion creep (n ≈ 1) for temperatures from 1020°C to 1110°C.

The values obtained allow to exclude the diffusion of O^{2-} in the anionic sub-lattice of Lu_2O_3, whose energy is 125 kJ.mol^{-1} in the temperature range 1020°C-1297°C **[36]**. No data about RE^{3+} (especially Lu^{3+}) diffusion activation energy in Lu_2O_3 is reported in literature, but Wang *et al.* have obtained a value for Y^{3+} grain boundary diffusion in Y_2O_3 equals to 410 kJ.mol^{-1} **[37]**. Finally, Gallardo-López *et al.* have found a value of 440 ± 70 kJ.mol^{-1} for creep tests controlled by grain boundary diffusion in Y_2O_3 ceramics **[38]**. As Y_2O_3 has the same structure and similar physico-chemical properties than Lu_2O_3, it can be supposed that such values should be similar to the activation energy of Lu^{3+} diffusion in Lu_2O_3. By considering the limited precision of the data reported here, it seems reasonable to conclude that the intermediate stage of densification is limited by Lu^{3+} diffusion at grain boundaries and can be similar to Coble creep.

3.4. Application to the manufacturing of highly transparent ceramics

Thanks to previous results regarding the determination of densification mechanism, an **interpretation of densification observed during a given** thermomechanical cycle is proposed in this study to manufacture highly transparent Ho:Lu_2O_3 ceramics suitable for laser applications. Such sintering schedule was reported in **Figure 13(a)**. In this case, the macroscopic stress is **being** applied during the entire heating (50°C.min^{-1}) after the regulation dwell at 600°C. The maximum temperature of 1400°C is maintained for 20 minutes with the maximum SPS uniaxial pressure of 50 MPa.

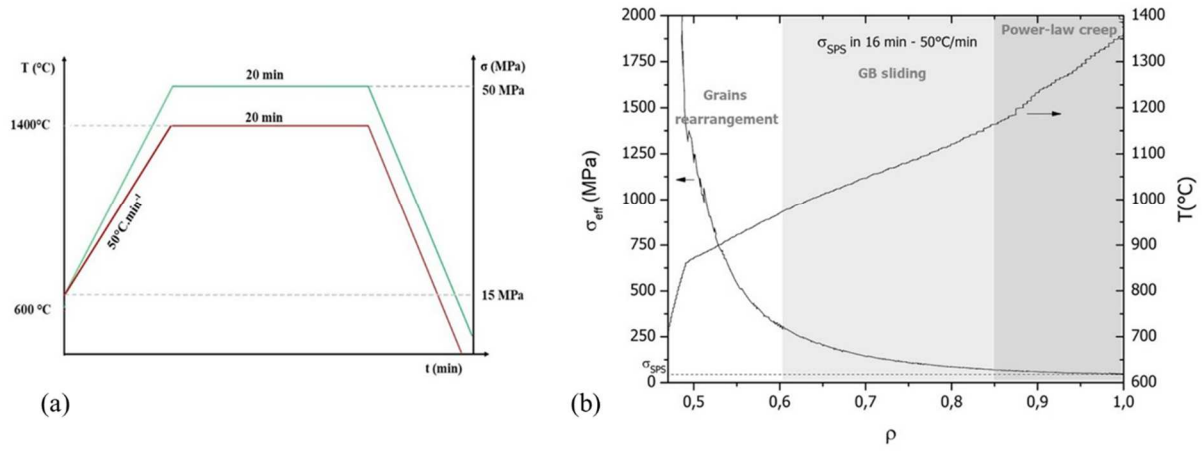

Figure 13. SPS thermo-mechanical cycle (a) and corresponding evolution of effective stress with associated densification mechanisms (b).

By calculating the corresponding effective stress according to Eq. (4) for the given sintering schedule, it was found that very high effective stress σ_{eff} of about 1.2 GPa is observed at the early beginning of sintering for ρ=0.5 (Figure 13(b)). Also in Figure 13(b) are reported the corresponding densification mechanisms determined from the previous paragraph. Grains rearrangement occurs in the first minutes of the sintering schedule whereas grain boundary sliding and creep should occur at higher densification stage, as expected from the densification model. Figure 14(a) presents the SEM micrograph and corresponding view of sample processed with the cycle presented in

Figure 13(a). This thermomechanical cycle leads to a homogeneous microstructure and absence of apparent porosity. As a conclusion, the thermomechanical cycle can be adapted to control effective stress; and by applying suitable schedule, homogeneous and perfectly dense microstructure can be obtained that is required for transparent ceramics manufacturing.

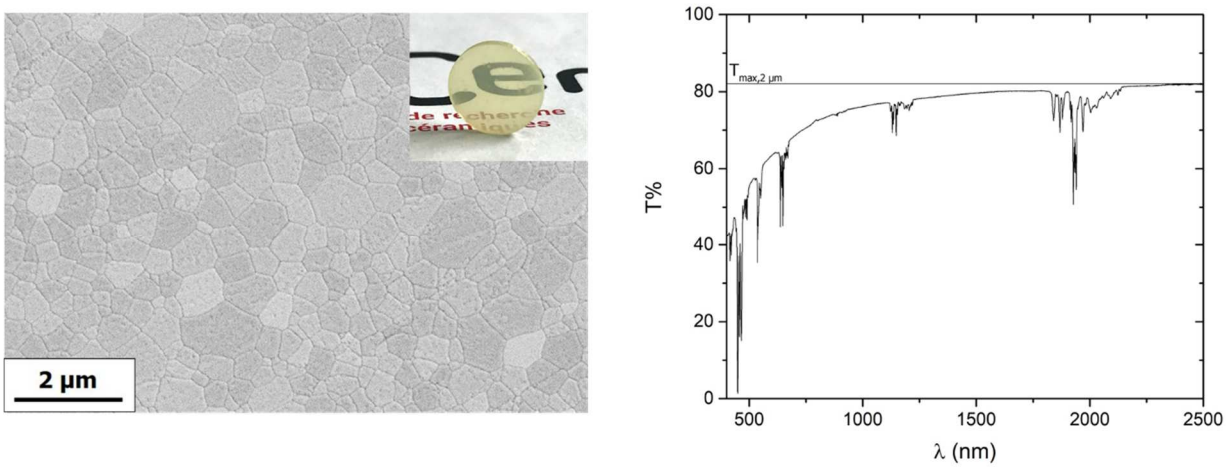

Figure 14. SEM micrographs and view of Ho:Lu_2O_3 sample sintered by SPS (a). Corresponding transmittance in Vis-IR wavelength range (b).

After sintering, reoxidation and polishing (**view of samples in Figure 14 (a)**), the optical transmission in visible-IR range of Ho:Lu_2O_3 sample was measured and results were reported in Figure 14(b). **The transmittance baseline at a wavelength of 1800-2200 nm is close to 80-81% that is very close the theoretical transmission at this wavelength (*i.e.* 81.6% calculated for a refractive index of 1.981).** It is well known that the optical transmission baseline decrease observed for wavelength inferior to 800 nm is linked to light scattering by residual porosity **[39], but the transmittance is not so much affected for wavelengths higher than 1500 nm**. This observation confirms the feasibility of obtaining good optical properties for Ho:Lu_2O_3 transparent ceramics, thanks to adapted SPS thermomechanical schedule. Owing to these first promising results, further works will be lead

on this topic by promoting one or another densification mechanism by making varying the thermomechanical SPS cycle.

Conclusions

This work have highlighted the strong evolution of densification controlling mechanism occurring during SPS sintering of Ho:Lu_2O_3 ceramics. The implementation of the constant microstructure approach indicated that for the first stage of densification (*i.e.* $\rho < 67\%$), a high value of stress exponent n was obtained (n around 3). This result was explained by the grain **rearrangement and coalescence known to be highly active for nanoparticles at early stage of sintering and evidenced in this study by microstructural investigations**. Then, for $67\% < \rho < 76\%$, a diffusion creep controlling mechanism by Rachinger sliding was found when n is around 2, followed by Lifshitz sliding ($76\% < \rho < 85\%$) with a stress exponent close to 1 and activation energy of 565 $kJ.mol^{-1}$. These last values are in accordance with a limiting mechanism by grain boundary diffusion of rare earth ions. At higher relative density ($\rho > 85\%$), power-law creep is involved meaning that densification is probably controlled by dislocations motion. Finally, this study allowed a better understanding of Ho:Lu_2O_3 ceramics densification during SPS sintering. **As a result, an adapted thermomechanical cycle was implemented to manufacture highly transparent Ho:Lu_2O_3 ceramics with homogeneous microstructure, low residual porosity, and high optical transmittance at a wavelength close to 2 µm. Such ceramics could be thus promising lasers hosts at such wavelengths.**

Acknowledgments

The authors are grateful to Pierre Carles (IRCER, Limoges, France) for TEM and STEM observations. This study was carried out with financial support of the Region

Nouvelle-Aquitaine (MISTRAL program n° 2017-1R50311) and was also supported by institutional grant from the National Research Agency under the Investments for the future program with the reference ANR-10-LABX-0074-01 Sigma-LIM.

References

[1] W.X. Zhang, J. Zhou, W.B. Liu, J. Li, L. Wang, B.X. Jiang, Y.B. Pan, X.J. Cheng, J.Q. Xu, Fabrication, properties and laser performance of Ho:YAG transparent ceramic, Journal of Alloys and Compounds Vol 506 (2010) 745–748.

[2] W.X. Zhang, Y.B; Pan, J. Zhou, W.B. Liu, J. Li, B.X. Jiang, X.J. Cheng, J.Q. Xu, Diode-Pumped Tm:YAG Ceramic Laser, Journal of the American Ceramic Society Vol 92 No 10 (2009) 2434-2437.

[3] K. Scholle, S. Lamrini, P. Koopmann and P. Fuhrberg, 2 µm Laser Sources and Their Possible Applications, Frontiers in Guided Wave Optics and Optoelectronics, Bishnu Pal, IntechOpen (2010).

[4] H. Yang, J. Zhang, X. Qin, D. Luo, J. Ma, D. Tang and Q. Zhang, Fabrication and properties of high quality transparent Ho:YAG ceramics, Solid State Phenomena Vol 185 (2012) 51-54.

[5] S.A. Payne, L.L. Chase, L.K. Smith, W.L. Kway, W.F. Krupke, Infrared cross section measurements for crystals doped with Er^{3+}, Tm^{3+}, and Ho^{3+}, IEEE J. Quantum Electron Vol 28 (1992) 2619-2630.

[6] Y. Wang, R. Lan, X. Mateos, J. Li, C. Hu, C. Li, S. Suomalainen, A. Härkönen, M. Guina, V. Petrov, and U. Griebner, Broadly tunable mode-locked Ho:YAG ceramic laser around 2.1 µm, Optics Express Vol 24 No 16 (2016) 18003-18012.

[7] H. Chen, D. Shen, J. Zhang, H. Yang, D. Tang, T. Zhao, X. Yang, In-band pumped highly efficient Ho:YAG ceramic laser with 21 W output power at 2097 nm, OPTICS LETTERS Vol 36 No 9 (2011) 1575-1577.

[8] X.J. Cheng, J.Q. Xu, M.J. Wang, B.X. Jiang, W.X. Zhang and Y.B. Pan, Ho:YAG ceramic laser pumped by Tm:YLF lasers at room temperature, Laser Physics Letters Vol 7 No 5 (2010) 351-354.

[9] R. Boulesteix, R. Epherre, S. Noyau, M. Vandenhende, A. Maître, C. Sallé, G. Alombert-Goget, Y. Guyot, A. Brenier, Highly transparent Nd:Lu_2O_3 ceramics obtained by coupling slip-casting and spark plasma sintering, Scripta Materialia Vol 75 (2014) 54–57.

[10] O.L. Antipov, A.A. Novikov, N.G. Zakharov, A.P. Zinoviev, Optical properties and efficient laser oscillation at 2066 nm of novel Tm:Lu_2O_3 ceramics, OPTICAL MATERIALS EXPRESS Vol 2 No 2 (2012) 183-189.

[11] A. Ikesue, Y.L. Aung, V. Lupei, Ceramic Lasers, Cambridge (2013) p.165.

[12] K. Serivalsatit, T. Wasanapiarnpong, C. Kucera, J. Ballato, Synthesis of Er-doped Lu_2O_3 nanoparticles and transparent ceramics, Optical Materials 35 (2013) 1426–1430.

[13] L. An, A. Ito, T. Goto, Fabrication of Transparent Lutetium Oxide by Spark Plasma Sintering, Journal of the American Ceramic Society Vol 94 No 3 (2011) 695–698.

[14] R. Orrù, R. Licheria, A. M. Locci, A. Cincotti, G. Cao, Consolidation/synthesis of materials by electric current activated/assisted sintering, Materials Science and Engineering R Vol 63 (2009) 127-287.

[15] S. Schwarz, O. Guillon, Two step sintering of cubic yttria stabilized zirconia using Field Assisted Sintering Technique/Spark Plasma Sintering, Journal of the European Ceramic Society Vol 33 (2013) 637-641.

[16] D.M. Hulbert, A. Anders, D.V. Dudina, J. Andersson, D. Jiang, C. Unuvar, U. Anselmi-Tamburini, E.J. Lavernia, A.K. Mukherjee, The absence of plasma in "spark plasma sintering", Journal of Applied Physics Vol 104 No 3 (2008) 033305.

[17] O. Yanagisawa, H. Kuramoto, K. Matsugi, M. Komatsu, Observation of particle behavior in copper powder compact during pulsed electric discharge, Materials Science and Engineering A Vol 350 No 1-2 (2003) 184-189.

[18] R. Raj, M. Cologna, J. Francis, Influence of Externally Imposed and Internally Generated Electrical Field on Grain Growth, Diffusional Creep, Sintering and Related Phenomena in Ceramics, Journal of the American Ceramic Society Vol 94 No 7 (2011) 1941-1965.

[19] J. Langer, M. Hoffmann, O. Guillon, Direct comparison between hot pressing and electric field-assisted sintering of submicron alumina, Acta Materialia Vol 57 No 18 (2009) 5454-5465.

[20] G. Bernard-Granger, N. Benameur, A. Addad, M. Nygren, C. Guizard, S. Deville, Phenomenological analysis of densification mechanism during spark plasma sintering of $MgAl_2O_4$, Journal of Materials Research Vol 24 No 6 (2009) 2011-2020.

[21] G. Bernard-Granger, C. Guizard, Spark plasma sintering of a commercially available granulated zirconia powder: I. Sintering path and hypotheses about the mechanism(s) controlling densification, Acta Materialia Vol 55 (2007) 3493-3504.

[22] A.S. Helle, K.E. Easterling, M.F. Ashby, Hot-isostatic pressing diagrams: New developments, Acta Metallurgica Vol 33 no 12 (1985) 2163-2174.

[23] G. Antou, P. Guyot, N. Pradeilles, M. Vandenhende, A. Maître, Identification of densification mechanisms of pressure-assisted sintering : application to hot pressing and spark plasma sintering of alumina, Journal of Materials Science Vol 50 (2015) 2327-2336.

[24] M.I. Mendelson, Average Grain Size in Polycrystalline Ceramics, Journal of The American Ceramic Society Vol 52 No 8 (1969) 443-446.

[25] B.-N. Kim, K. Hiraga, K. Morita, H. Yoshida, Y.-J. Park, and Y. Sakka, Dynamic grain growth during low-temperature spark plasma sintering of alumina, Scripta Materialia, 80 29–32 (2014).

[26] B.-N. Kim, K. Hiraga, S. Grasso, K. Morita, H. Yoshida, H. Zhang, and Y. Sakka, High-pressure spark plasma sintering of MgO-doped transparent alumina, Journal of the Ceramic Society of Japan, 120 [1399], 116–118 (2012).

[27] O. Ünal, M. Akinc, Compressive Properties of Yttrium Oxide, Journal of the American Society Vol 79 No 3 (2005) 805 – 808.

[28] E. Calvié, J. Réthoré, L. Joly-Pottuz, S. Meille, J. Chevalier, V. Garnier, Y. Jorand, C. Esnouf, T. Epicier, J.B. Quirk, et al., Mechanical behavior law of ceramic nanoparticles from transmission electron microscopy in situ nano-compression tests, Materials Letters, 119 107–110 (2014).

[29] E. Calvié, L. Joly-Pottuz, C. Esnouf, P. Clément, V. Garnier, J. Chevalier, Y. Jorand, A. Malchère, T. Epicier, and K. Masenelli-Varlot, Real time TEM observation of alumina ceramic nano-particles during compression, Journal of the European Ceramic Society, 32 [10], 2067–2071 (2012).

[30] R. Chaim, M. Kalina, J.Z. Shen, Transparent yttrium aluminum garnet (YAG) ceramics by spark plasma sintering, Journal of the European Ceramic Society Vol 27 (2007) 3331-3337.

[31] R. Chaim, Densification mechanisms in spark plasma sintering of nanocrystalline ceramics, Materials Science and Engineering A Vol 443 (2007) 25-32.

[32] R. Chaim, M. Levin, A. Shlayer, C. Estournès, Sintering and densification of nanocrystalline ceramic oxide powders: a review, Advances in Applied Ceramics Vol 107 No 3 (2008) 159-169

[33] W.R. Cannon, T.G. Langdon, Review creep of ceramics, Journal of Materials Science, Vol 18 (1983) 1-50

[34] O. Guillon, J. Gonzalez-Julian, B. Dargatz, T. Kessel, G. Schierning, J. Rathel, M. Hermann, Field-Assisted Sintering Technology/Spark Plasma Sintering: Mechanisms, Materials, and Technology Developments, Advanced Engineering Materials Vol 16 No 7 (2014) 830-849.

[35] G. Antou, N. Pradeilles, M. Gendre, A. Maître, New approach of the evolution of densification mechanisms during Spark Plasma Sintering: Application to zirconium (oxy-)carbide ceramics, Scripta Materialia Vol 101 (2015) 103-106.

[36] M.F Berard, C.D. Wirkus. D.R. Wilder, Diffusion of Oxygen in Selected Monocrystalline Rare Earth Oxides, Journal of the American Ceramic Society Vol 51 No 11 (1968) 643-647.

[37] X.-H. Wang, P.-L. Chen, L.-W. Chen, Two-step sintering of ceramics with constant grain-size, I, Y_2O_3, Journal of the American Ceramic Society Vol 89 (2006) 431-437.

[38] A. Gallardo-López, A. Domínguez-Rodríguez, C. Estournès, R. Marder, R. Chaim, Plastic deformation of dense nanocrystalline yttrium oxide at elevated temperatures, Journal of the European Ceramic Society Vol 32 (2013) 3115-3121.

[39] R. Boulesteix, A. Maître, J.-F. Baumard, Y. Rabinovitch, F. Reynaud, Light scattering by pores in transparent Nd:YAG ceramics for lasers: correlations between microstructure and optical properties, Optics Express Vol 18 No 14 (2010) 14992-15002.